STATIC AND ROTORDYNAMIC ANALYSIS OF A PLAIN ANNULAR (LIQUID) SEAL IN THE LAMINAR REGIME WITH A SWIRL BRAKE FOR THREE CLEARANCES

Ovais Ahmed Bin Najeeb
Turbomachinery Laboratory
Texas A&M University
College Station, TX 77843, USA

Dara W. Childs
Leland T. Jordan Professor of
Mechanical Engineering
Texas A&M University
College Station, TX 77843, USA

ABSTRACT

Annular seals are non-contacting mechanical elements designed to reduce leakage between two areas of differing pressures such as between two impeller stages in a pump. Circumferential fluid rotation inside the annular liquid seals is the leading cause of pump rotordynamic instabilities. Swirl brakes have been shown to be effective in reducing fluid rotation at the inlet of the seal; thus reducing destabilizing forces in the seal. Data showing the effects of swirl brakes over a range of clearance-to-radius ratios in *laminar fluid flow* conditions are needed.

This study involves tests using a smooth seal with three radial clearances $C_r = 127\mu m, 254\mu m, 381\mu m$ (1X, 2X and 3X respectively), an axial length of 45.72 mm (1.80 in) and a diameter of 101.6 mm (4.00 in). An insert was used to induce pre-swirl upstream of the seal. Swirl brakes (SBs) were used to reduce circumferential fluid flow at the seal inlet. Swirl brakes comprised 36 square cuts at the seal entrance with an axial depth of 5.08 mm (0.2 in), radial height of 6.35 mm (0.25 in) and circumferential width of 6.35 mm (0.25 in) each. The study produced static and rotordynamic data at ω = 2, 4, 6, 8 krpm, ΔP = 2.07, 4.14, 6.21, 8.27 bar (30, 60, 90, 120 psi), and eccentricity ratios $\varepsilon_0 = e_0/C_r$ = 0.00, 0.27, 0.53, and 0.80. The test used ISO VG 46 oil at a range of 115-120 °F to keep f the fluid flow laminar (Total $Re \leq 650$). Dynamic measurements included components of the following vectors (a) stator-rotor relative displacements, (b) acceleration and (c) applied dynamic force in the *X-Y* coordinate system. Measurements were also compared to predictions from a code developed by Zirkelback and San Andrés [1].

SBs are shown to be effective in minimizing inlet fluid rotation at the 3X clearance but ineffective at the 1X and 2X clearance. When SBs are used with the 3X clearance seal, the cross-coupled stiffness variables have the same sign meaning that the seal would have a WFR of zero and would not produce destabilizing forces on a pump rotor. However, at the 3X clearance, the smooth annular seal has a negative direct stiffness K that could potentially "suck" the rotor into contact with the stator wall, along with dropping the natural frequency of the pump rotor, further reducing its dynamic stability. Most of the predictions agree well with the test data. Notable exceptions are the direct and cross-coupled stiffness coefficients for the 3X clearance. Predictions showed positive direct stiffness and opposite signs for the cross-coupled stiffness coefficients.

NOMENCLATURE

C_r	Seal radial clearance [L]
D	Seal diameter [L]
F_s	Required applied static load [F]
f_t, f_r	Seal reaction forces in t and r directions [F]
k	Cross-coupled stiffness coefficient [M/T^2}
L	Seal axial length [L]
$\dot{Q}$	Seal volumetric leakage rate [L^3/T]
R	Shaft radius [L]
ΔP	Seal differential pressure [F/L^2]
v_i	Inlet circumferential fluid velocity [L/T]
v_{insert}	Fluid velocity leaving the pre-swirl insert [L/T]
ε_0	Static eccentricity ratio [-]
ω	Rotor speed [1/T]
1X,2X,3X	New radial clearance, two times the new radial clearance and three times the new radial clearance [-]
ϕ	Attitude angle shown in figure 18.

Subscripts

i, j	Interchangeable X and Y directions
r, t	Radial and tangential components

Abbreviations

PSR	Pre-swirl ratio, defined in Eq. (5)
SBs	Swirl brakes
SSSB	Smooth seal with swirl brakes
WFR	Whirl frequency ratio

INTRODUCTION

Pumps and compressors use annular seals to reduce leakage between regions of differing pressures. Annular seals are non-contacting; there is a clearance between the rotor and the seal stator.

Shaft centering forces are developed in annular seals by mainly two means, (1) the hydrodynamic effect (fluid rotation), and, (2) the Lomakin effect [2]. Starting with the hydrodynamic effect, the eccentric position of the shaft in the annulus produces a converging region where pressure is higher and a diverging region where pressure is lower. The difference in circumferential pressure distribution produces a shaft reaction force. The hydrodynamic effect is pronounced in hydrodynamic bearings where shear flow due to shaft rotation is dominant due to lower C_r/R ratios. The hydrodynamic effect is discussed in detail by Pinkus and Sternlicht [3].

Figure 1 helps in explaining the Lomakin effect [2]. Initially, the rotor is centered in the seal. The high $\Delta P = P_{supplied} - P_{exit}$ causes the fluid to accelerate at the inlet. This leads to a pressure drop at the seal entrance followed by a pressure drop through the seal due to wall friction. As the rotor is displaced from the center of the seal, the clearance at the top decreases, leading to lower axial velocity, lower Reynolds number, and higher friction factor. Whereas, the clearance at the bottom increases, which leads to higher axial velocity, higher Reynolds number, and lower friction factor. A combination of these factors results in an axial pressure distribution (shown as gray areas in FiG. 1) that leads to a resultant centering force, F.
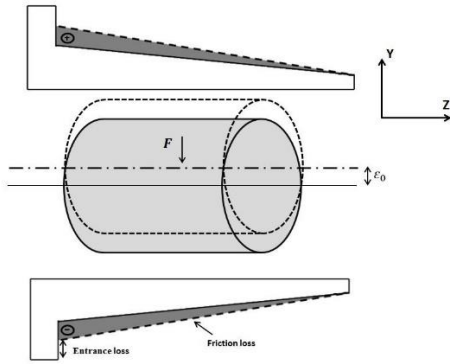

Figure 1. Lomakin effect.

The flow inside the seal can be stated in terms of an average circumferential component and an average axial component with a corresponding circumferential Reynolds number (Re_c) and axial Reynolds number (Re_a), respectively. Total Reynolds number, Re_t refers to the resultant of Re_c and Re_a. For an annular seal the hydraulic diameter is $2C_r$. Hence,

$$Re_c = \frac{\rho R \omega C_r}{\mu} \tag{1}$$

$$Re_a = \frac{\rho 2(C_r) w}{\mu} \tag{2}$$

$$Re_t = \sqrt{Re_a^2 + Re_c^2}, \tag{3}$$

where μ is lubricant viscosity and $w = \dot{Q}/2\pi RC_r$ is the average axial velocity. At tighter clearances and laminar flow conditions ($Re_t < 1800$), seals generally act more like bearings as fluid rotation effects dominate.

For Electric Submersible Pumps (ESPs), as the clearances increase, viscous forces due to fluid rotation decrease, and the Lomakin effect becomes more pronounced even when the fluid flow is laminar [4].

Instability in a rotor-bearing system is primarily caused by fluid rotation in the bearing/seal annulus [5]. Black et al. [6] were the first to analyze the effect of inlet pre-swirl of the fluid flow on the seals' rotordynamic characteristics. Figure 2 from Childs [5] shows the predicted WFR (WFR=$k/C\omega$) versus length to diameter ratio, L/D, of a seal ($C_r/R = 0.005$) with changing inlet pre-swirl. WFR drops as inlet/pre-swirl decrease. The cross coupling stiffness coefficient k is also a function of the inlet pre-swirl, and it decreases as inlet swirl drops [5]. A lower WFR and k thus would reduce the seal's ability to destabilize a pump.
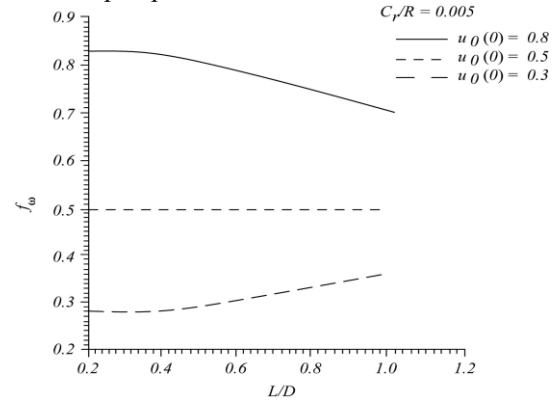

Figure 2. Effect of changing Inlet Swirl on WFR for a Smooth Seal [5].

SBs use a series of circumferential slots or webs at the seal inlet to lower the inlet pre-swirl of the fluid entering a seal. Benchert and Wachter [7] were the first to use SBs for gas labyrinth seals, referring to them as "swirl webs" to effectively reduce WFR and k.

Figure 3 shows an SB design used by Massey [8] to stabilize a pump. Massey's pump operated with a light hydrocarbon with low viscosity at elevated temperatures. It was unstable, and an SB at the balance-piston seal was required to stabilize it. SBs have been shown to be effective in machines handling low viscosity fluids such as Massey's pump. On the other hand, the effectiveness of installing SBs on seals operating with higher viscosity fluids is still uncertain.
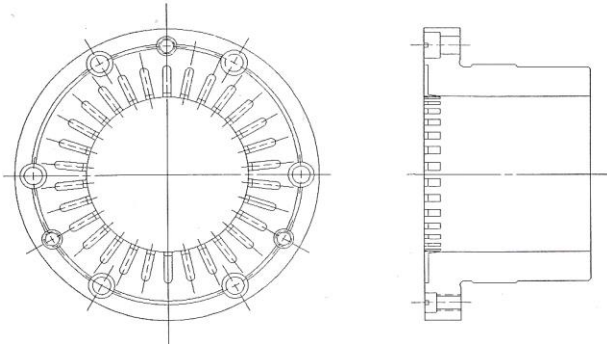
Figure 3. Balance-piston seal swirl brake [5].

With a high-viscosity liquid at low seal clearances, shear forces due to shaft rotation are large and overwhelm the inlet pre-swirl condition, and the bulk-flow circumferential velocity is $R\omega/2$. SBs are predicted to be ineffective in these conditions. As clearance and leakage increase due to wear in a pump, the hydrodynamic effect becomes less effective, and the Lomakin effect becomes more important. Using predictions from the model of [1] for seal rotordynamic coefficients, Childs and Norrbin [4] predicted that SBs would be effective in improving the rotordynamic stability of seals in these enlarged-clearance circumstances. This study aims to experimentally investigate the predictions of seal rotordynamic coefficients of smooth seals with SBs, operating with a higher viscosity fluid at enlarged clearances.

This study presents measurements of the static and rotordynamic force coefficients for a smooth seal with swirl brakes (SSSB) for the first time in the laminar flow regime. Measurements are also compared to predictions by a code based on Zirkelback and San Andrés [1]. Additionally, imposed pre-swirl immediately upstream of swirl brake and outlet swirl are measured. The first author conducted this study as part of a Master's thesis at Texas A&M University. Details of the literature review, test rig, testing procedure, data analysis, and results can be found in Ref. [9].

The test seals use SBs and are smooth with axial length $L=$ 45.720 mm (1.800 in) and clearances $C_r =$ $127\mu m, 254\mu m, 381\mu m$ (1X, 2X and 3X respectively). The corresponding radial clearance to radius ratios (C_r/R) were 0.0025, 0.005, 0.0075. The length to diameter ratio (L/D) of the annular seal was 0.45. Figure 4 presents a detailed drawing of the seal with SBs. Each SB has a total of 36 square cuts with axial length $D_{sb} =$ 5.08 mm (0.2 in), radial height $H_{sb} =$ 6.35 mm (0.25 in) and circumferential width $W_{sb} =$ 6.35 mm (0.25 in).
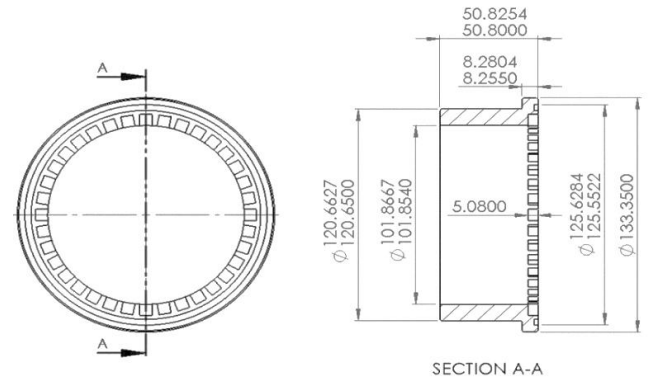

Figure 4. Detailed drawing of new clearance seal with swirl brakes. All dimensions are in mm

The seal test matrix consists of 192 test points:
3 Clearances: 1X, 2X and 3X,
4 running speeds: 2, 4, 6, and 8 krpm,
4 axial pressure drops: 2.07, 4.14, 6.21, and 8.27 bar,
4 eccentricity ratios: 0.00, 0.27, 0.53, and 0.80.
ISO VG 46 oil is used as the test fluid at a temperature range of 46.0-49.0 ℃.

TEST APPARATUS

The test rig shown in Fig. 5 was used to conduct static and dynamic measurements of the SSSBs. It was initially designed by Kaul [10] to test annular oil bushing seals for compressors. "Ground" for the main test section is formed by mild steel plates that support the electric motor, the motor mount and the two pedestals.
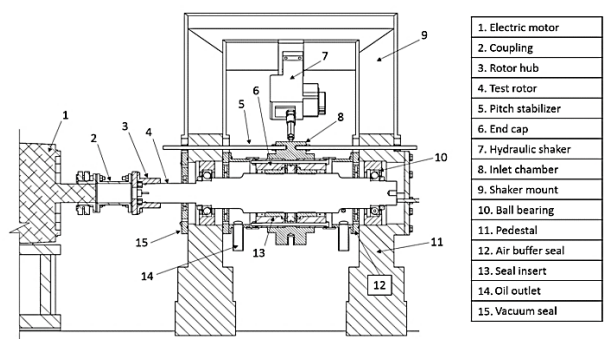

Figure 5. Cross-sectional view of the main test section.

The pedestal assemblies have an upper half and a lower half. The lower half supports angular contact ball bearings that in turn support the smooth rotor with a span of 640.1 mm (25.2 in) and maximum diameter of 101.6 mm (4 in). The rotor is connected to the variable frequency drive 29.8 kW (40 hp) electric motor by the coupling. The rotor maximum speed is 8 krpm. As shown in Fig. 5 and described in detail in [10], other peripherals that form the main test section include pitch stabilizers, collection chambers, an end cap, air buffer seals and vacuum seal. Pitch stabilizers are 6 long threaded bolts that are screwed between the pedestals and the stator to keep the stator

parallel to the rotor [10]. The collection chambers collect the oil as it leaves the stator during testing. An end cap seals the non-drive end (NDE) of the main test section.

The upper half of the pedestal assembly contains the two hydraulic shaker assemblies. Shaker heads are connected to the stator via stingers as shown in Fig. 6. The hydraulic shaker assembly includes a load cell mounted on each of the orthogonal X and Y axes to measure the force applied in each direction. The shakers can excite the stator up to 1kHz and provide a maximum tension and compression of 4450 N.
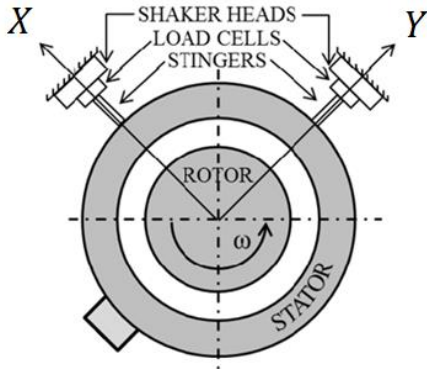

Figure 6. Drive Side (DS) view of the shaker assembly. Adapted from [10].

Figure 7 is a photo of the 1X clearance test seal. The SB design is inspired from Massey's SB design [8] as shown previously in Fig. 3. Its rugged construction would resist wear due to particulates in the flow. A better design for inlet circumferential flow control could probably be developed using CFD. With the data provided in this study, the design could be further improved using CFD analysis.

Figure 7. 1X clearance seal with SBs.

Figure 8 shows the insert used to induce pre-swirl. The insert has 12 nozzles. Each nozzle has a diameter of 4.039 mm (0.1590 in). It was designed to produce inlet pre-swirl ratio (defined in Eq. (5)) ranging from 0-0.8 depending on rotor

speed and ΔP. Note that the injection angle is such that the fluid stream leaving the pre-swirl insert nozzles is tangential to the rotor surface as shown in Fig. 8.
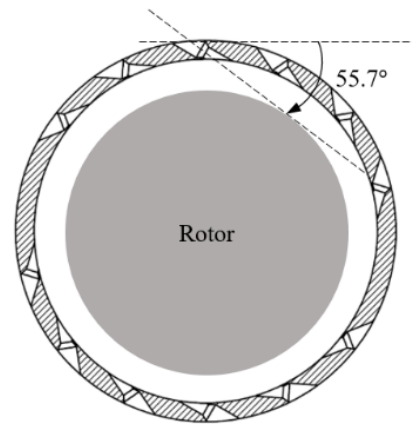

Figure 8. Cross-sectional view of high pre-swirl insert.

As shown in Fig. 9, the stator assembly consists of the following three main parts: inlet chamber, seal holders, and SSSBs. The pre-swirl insert described above is part of the inlet chamber. SSSBs are press fitted into a set of seal holders that are in turn assembled into the inlet chamber.
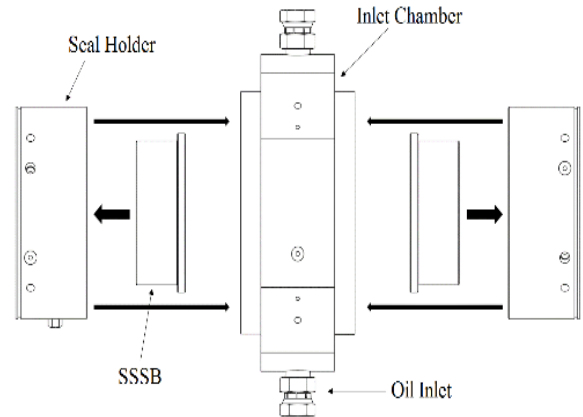

Figure 9. Stator assembly schematic.

Figure 10 shows the test-fluid flow path. After passing through the pre-swirl insert, the swirling fluid is then met by the SBs. Oil then enters the seals and eventually leaves the stator into the collection chambers. Note that a labyrinth tooth at the end of the seal holder is present to avoid cavitation at the seal's exit.
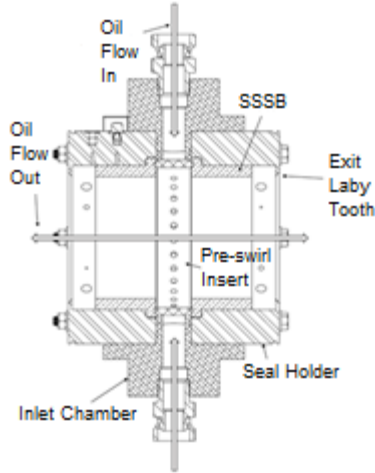
Figure 10. Stator and lubricant flow path.

The instrumentation shown in Fig. 11 was used to measure the dynamic and static characteristics of the test rig.
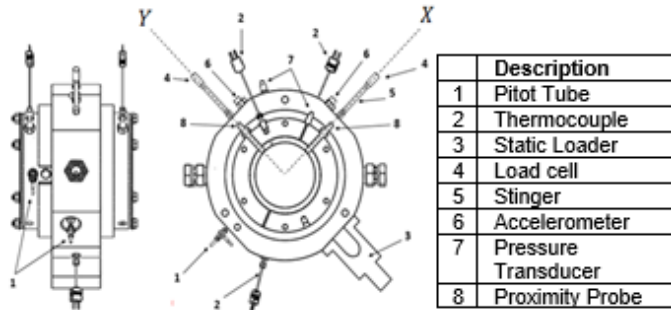

	Description
1	Pitot Tube
2	Thermocouple
3	Static Loader
4	Load cell
5	Stinger
6	Accelerometer
7	Pressure Transducer
8	Proximity Probe

Figure 11. Assembled stator and instrumentation.

STATIC TEST PROCEDURE

Prior to tests, the "Cold" clearance of the seal is measured without any oil in the system at zero ω. Cold refers to the measurement that is taken at room temperature. As shown in Fig. 11, Four-eddy current sensors, located orthogonally in two different axial planes, measure the gaps between the seal and rotor (radial clearance). To measure the clearance circle, the seal housing is forced to touch the rotor with an applied force from the hydraulic shakers. The housing is then precessed 360° around the rotor by adjusting the force from X and Y shaker units while maintaining a contact force. Continuous acquisition of the clearance data throughout this process captures the clearance circle of the test seal. The cold-clearance circle also locates the geometric center of the seal.

The operator supplies oil to the test-rig oil until (using a heater) the lubricant temperature reaches a steady test condition of 46.1°C (115±5°F). At this point, oil flow is stopped, and the clearance circle is immediately measured. This clearance circle is the "hot" clearance circle. It is smaller than the cold clearance circle due to thermal expansion. The hot clearance is used to calculate the eccentricity ratios.

At each steady-state condition, sensors are used to measure the following parameters: ω, ΔP, eccentricity (e_0, relative rotor position in the X and Y coordinate system), inlet and outlet temperatures, Leakage ($\dot{Q}$), and applied static load (F_s). Note that the measured values of $\dot{Q}$ and F_s are for both of the back-to-back test seals. They need to halved to get values for each seal.

STATIC RESULTS

Leakage

Figure 12 shows predicted and measured $\dot{Q}$ versus ε_0 at (a) ΔP = 2.07 and (b) ΔP = 8.27 bar and for all clearances. An in-house code, XLanSeal® based on a model discussed in [1] is used for predictions. Note that Exp X and XLan X in the graph refer to measured and predicted $\dot{Q}$ for the 1X clearance seal, respectively, and the naming convention is repeated for the 2X and 3X clearance seal. Uncertainty values are very small compared to measured data and are difficult to see in the figure. As expected, $\dot{Q}$ increases as C_r and ΔP increase. $\dot{Q}$ is predicted well for the 1X and the 2X clearance seals. However, measured $\dot{Q}$ is 1.25 times higher than predicted $\dot{Q}$ for the 3X clearance seal.

Note that ΔP was obtained using a pressure measured upstream of the SBs and not immediately upstream of the seal inlet. The same ΔP was used to predict $\dot{Q}$ across the seal. The $\dot{Q}$ discrepancy between measurements and predictions could be due to the SBs converting the velocity head due to circumferential flow into a pressure head, thereby increasing the ΔP across the seal. However, assuming that the inlet circumferential velocity head $\rho v_i^2/2$ is converted to pressure, the $\dot{Q}$ predictions for the 3X clearance seal do not significantly improve.
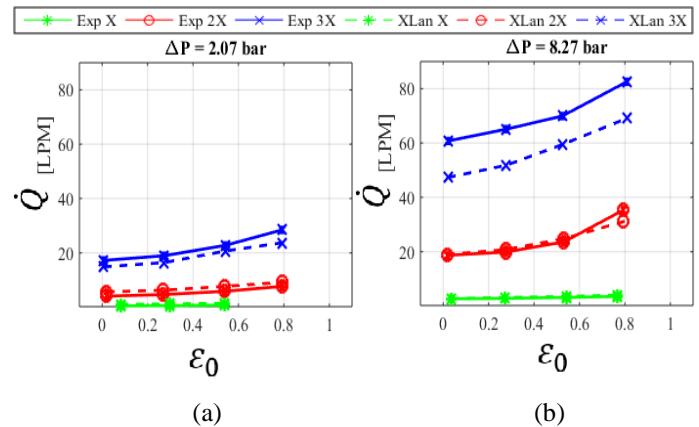

Figure 12. Measured and predicted $\dot{Q}$ versus ε_0 for ω = 6 krpm at (a) ΔP = 2.07 bar, and (b) ΔP = 8.27 bar.

Pre-swirl Ratio

Two pitot tubes measure the dynamic and static pressure at the inlet and outlet of the liquid annular seal. They are used to

calculate the inlet and outlet circumferential velocities (v_i and v_o), respectively at specific locations. The defining equation is

$$v = \sqrt{\frac{2\Delta P_{pitot}}{\rho}} \qquad (4)$$

where ΔP_{pitot} is the pressure difference between the static and dynamic pressure measurements, and ρ is the fluid density. The swirl ratio is the ratio of the fluid inlet circumferential velocity to the rotor's surface speed. The pre-swirl ratio (PSR) is

$$PSR = \frac{v_i}{\omega R} \qquad (5)$$

Figure 13a shows the axial positions of the inlet and outlet pitot tubes. Figure 13b shows an enlarged axial view of the inlet pitot tube.
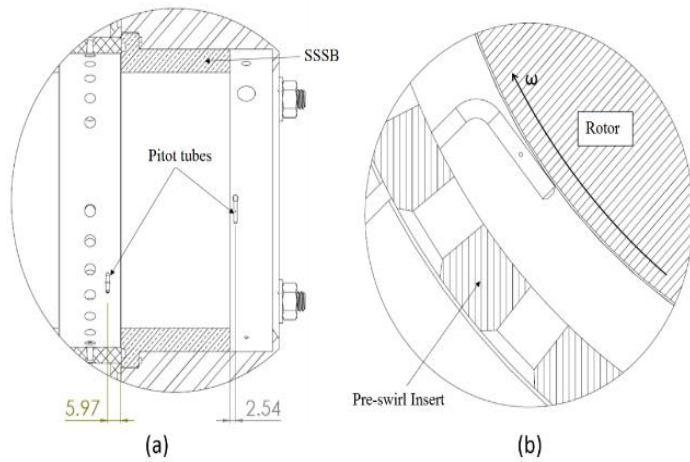

Figure 13. (a) Axial positions of the pitot tubes. (b) Radial view of the inlet pitot tube location. All dimensions in mm. Adapted from [11].

Figure 14 shows the location of the pre-swirl pitot tube. Note that the radial location of the pre-swirl pitot tube differs for each of the SSSBs. The pre-swirl pitot-tube radial clearance always equals the radial clearance C_r of the seal; specifically 0.127, 0.254 and 0.381 mm for 1X, 2X and 3X C_r, respectively.
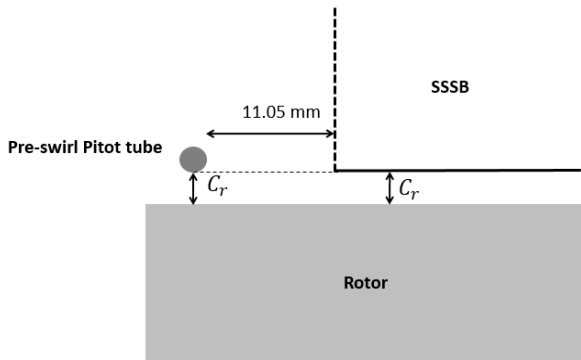

Figure 14. Radial position of the inlet pre-swirl pitot tube. Note that the Figure is not drawn to scale.

Figure 15 shows the measured inlet circumferential velocity v_i versus ω for a range of ΔP. The solid lines represent measured v_i. The dashed lines represent the fluid velocity leaving the pre-swirl insert, v_{insert} calculated as follows

$$v_{insert} = \frac{\dot{Q}}{12\pi r_{nozzle}^2} \qquad (6)$$

where r_{nozzle} is the radius of each hole in the pre-swirl insert.

The darkest line represents $R\omega$, the fluid circumferential velocity at the rotor surface assuming no slip conditions. Figure 15 shows that v_i increases as ω and ΔP increase for all the clearances. The v_i magnitudes are higher than v_{insert}, especially for the 2X and the 3X clearance seals. For the 3X clearance seal, v_{insert} is higher than v_i at ω = 2krpm and all ΔPs. The data of Fig. 15 shows a slight relationship between v_{insert} and v_i to the extent that generally v_i (3X) > v_i (2X) > v_i (1X) but changes in ω have a clear impact on v_i. One explanation for this impact is the induced circumferential flow due to shaft rotation, particularly with the high fluid viscosity used here. Another possible explanation could be the location of the pitot tube. As C_r increases, the distance between the pitot tube and the rotor also increases (refer to Fig. 14). Thus the fluid velocity measurement location changes from seal to seal. v_i does increase with increasing ω indicating an induced pre-swirl due to shearing force from the shaft rotation. As ΔP increases, v_i tends to trend more with v_{insert} and less with $R\omega$. v_i is closer to the average fluid circumferential velocity ($R\omega/2$) for the 3X clearance seal.

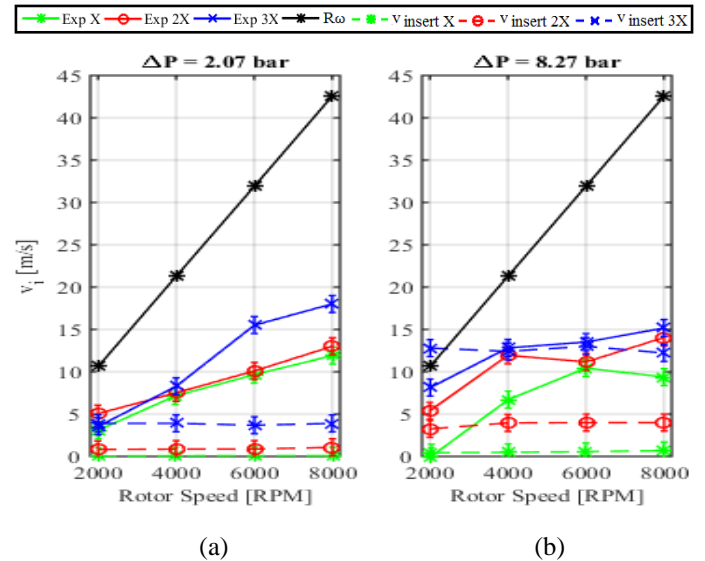**Figure 15. v_i versus ω at ε_0 = 0.00 and (a) ΔP = 2.07 bar and (b) ΔP = 8.27 bar.**

Figure 16 shows PSR versus ω at the centered position. As expected from Eq. (5), PSR generally decreases with increasing ω for all the seal clearances even though Fig. 15 shows v_i increasing as ω increases.
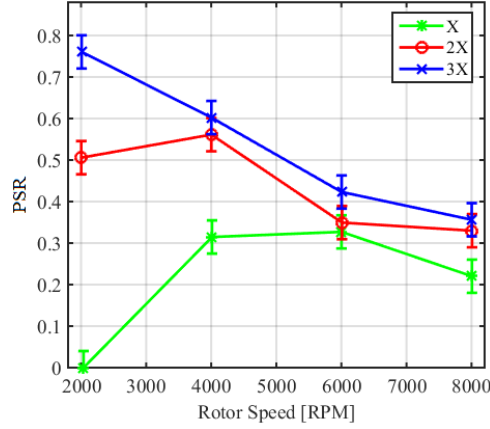
Figure 16. PSR versus ω at ΔP = 8.27 bar.

LOAD AND POSITION CONTROL

Dynamic measurements at various eccentricity ratios can be set from the test rig in the following two modes: (a) Load Control, (b) Position control. As shown in Fig. 17a, load control refers to a force F_s being applied by the shaker to the stator in the $-Y$ direction with no force being applied through the X-axis to achieve a specified ε_0. Alternatively, as shown in Fig. 17b, to achieve a specified ε_0, the shaker heads are used directly to position the stator along the Y axis by applying forces from both shaker heads. The basic aim is to get the same ε_0 using either scheme. Most of the seals can be tested in the load-control mode as the seal-rotor system achieves an equilibrium position at a certain ε_0 and F_s. For some conditions, testing cannot be performed in load-control as the seal becomes statically unstable. However, such seals can be tested using the shakers in position control. The shakers in the X and Y direction provide the force components that are required to keep the stator in a specified eccentric position.
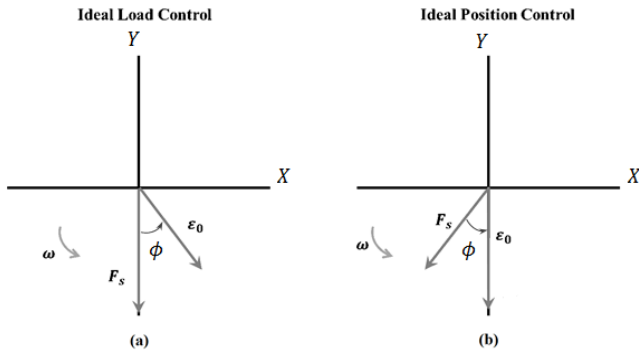

Figure 17. (a) Ideal load control, (b) Ideal position control.

The 1X and 2X clearance seals were tested in load-control. The 3X clearance seal was tested in position control. To compare the 1X, 2X and 3X clearance seal resuts, the auhors used the $\boldsymbol{\epsilon_r}$ and $\boldsymbol{\epsilon_t}$ coordinate system. As shown in Fig. 18, the eccentricity vector is always in the $\boldsymbol{\epsilon_r}$ direction.
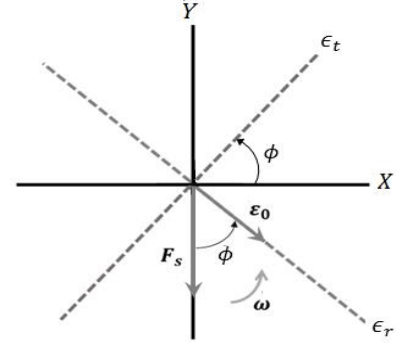

Figure 18. Coordinate transformation from cartesian coordinate system to r and t coordinate system.

The following similarity transformation is used to transform dynamic- coefficients in the X-Y cartesian coordinate system to the r-t system.

$$\begin{bmatrix} Z_{tt} & Z_{tr} \\ Z_{rt} & Z_{rr} \end{bmatrix} = \begin{bmatrix} \cos\phi & \sin\phi \\ -\sin\phi & \cos\phi \end{bmatrix} \begin{bmatrix} Z_{XX} & Z_{XY} \\ Z_{YX} & Z_{YY} \end{bmatrix} \begin{bmatrix} \cos\phi & -\sin\phi \\ \sin\phi & \cos\phi \end{bmatrix} \tag{7}$$

where ϕ, illustrated in Fig.18, is the angle between the $\boldsymbol{F_s}$ and $\boldsymbol{\varepsilon_0}$ vector. The transformation applies to the [K], [C], and [M] matrices. The rotordynamic model using the $\boldsymbol{\epsilon_t}$ and $\boldsymbol{\epsilon_r}$ coordinate system is

$$-\begin{Bmatrix} f_t \\ f_r \end{Bmatrix} = \begin{bmatrix} K_{tt}(e_0) & K_{tr}(e_0) \\ K_{rt}(e_0) & K_{rr}(e_0) \end{bmatrix} \begin{Bmatrix} x_t \\ x_r \end{Bmatrix} + \begin{bmatrix} C_{tt}(e_0) & C_{tr}(e_0) \\ C_{rt}(e_0) & C_{rr}(e_0) \end{bmatrix} \begin{Bmatrix} \dot{x}_t \\ \dot{x}_r \end{Bmatrix}$$

$$+ \begin{bmatrix} M_{tt}(e_0) & M_{tr}(e_0) \\ M_{rt}(e_0) & M_{rr}(e_0) \end{bmatrix} \begin{Bmatrix} \ddot{x}_t \\ \ddot{x}_r \end{Bmatrix} \tag{8}$$

Required Applied Static Load and Attitude Angle

Figure 19a shows measured attitude angle ϕ versus ε_0 at ω = 8krpm and ΔP = 2.07 bar. At $\varepsilon_0 = 0.00$, ϕ could not be determined because both the force and eccentricity vectors were zero. As expected, for the 1X clearance seal at $\varepsilon_0 = 0.27$, $\phi \geq 90°$ is an indication that fluid inertia effects are important [12]. Destabilizing circumferential forces exist, and there is presence of decentering forces. As expected, for the 1X seal, ϕ generally decreases as ε_0 increases. At $\varepsilon_0 > 0.27$, ϕ is less than 90°, suggesting a positive centering force and a transverse force in the ω direction. For the 2X clearance seal at $\varepsilon_0 = 0.27$, $\phi \cong$ 90°. In such a situation, no centering force component exists; only a destabilizing force component exists. ϕ decreases as ε_0 increases and remains unaffected by a change in ΔP. For the 3X clearance seal, $\phi \cong 180°$ at $\varepsilon_0 = 0.27, 0.53$, implying that there is no forward circumferential destabilizing force, and that the centering force is negative. $\phi < 90°$ for all other test conditions.

Figure 19b shows the measured and predicted static load F_s required to produce each specified ε_0 for all clearances and ΔPs. While testing in load control, the load F_s is increased to

achieve a specified ε_0; hence, for the 1X and 2X clearance seals, required F_s is a function of ε_0 not vice versa. F_s increases as ε_0 increases and C_r decreases. There is generally good agreement between predictions and measurements. However for the 1X clearance seal at ε_0 = 0.80, measured F_s is consistently larger than predicted. For the 3X clearance at ε_0 = 0.23, 0.57 at ΔP = 2.07 bar and ω = 8krpm, measured F_s is negative. This outcome agrees with the ϕ = 180° results shown in Fig. 19a. Direct stiffness would be expected to be negative in these cases. The model fails to predict negative F_s at ε_0 = 0.23, 0.57 at ΔP = 2.07 bar and ω = 8krpm. Note that the uncertainties are small and difficult to see in the figure.
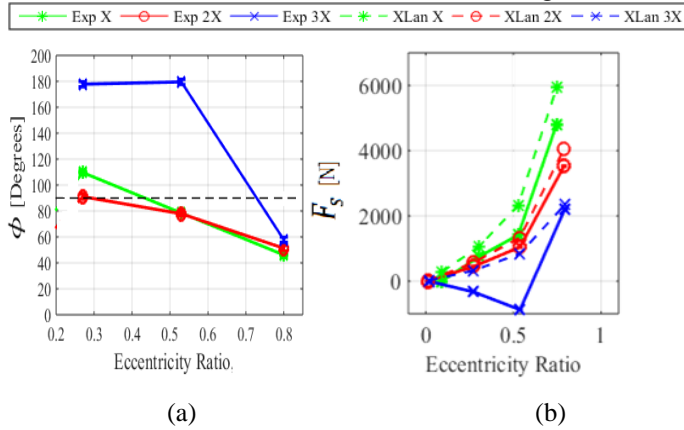

Figure 19. ω = 8krpm and ΔP = 2.07 bar (a) Measured ϕ versus ε_0, (b) Measured F_s versus ε_0.

ROTORDYNAMIC - COEFFICIENT PARAMETER IDENTIFICATION

The multiple-frequency-excitation method employed by Rouvas and Childs [13], and Childs and Hale [14] was used here to measure the seal dynamic-stiffness coefficients. The input shake frequency is a pseudo random waveform optimized to provide maximum excitation at a range of frequencies between ~10-200 Hz. The stator acceleration components, relative rotor stator displacement components, and applied dynamic load components are measured as the hydraulic shakers excite the stator in each of the orthogonal (X & Y) directions. The force, acceleration, and relative-displacement data components obtained in the time domain are transformed into the frequency domain using the fast Fourier transform (FFT) method. The real and imaginary parts of the complex frequency response function, $\boldsymbol{H_{ij}}$ can be related to the stiffness, damping and virtual-mass coefficients by

$$\boldsymbol{H_{ij}} = \left(K_{ij} - \Omega^2 M_{ij}\right) + \boldsymbol{j}(\Omega C_{ij}) \qquad (9)$$

where Ω is the excitation frequency and $\boldsymbol{j}$ is $\sqrt{-1}$. Next, least-squares regression curve fits are applied to the real and imaginary parts of the complex frequency response function. The coefficients from these curve fits produce the stiffness, damping and virtual mass terms. For repeatability calculations,

a 95% confidence interval is used. Confidence intervals for the rotordynamic coefficients are calculated using a statistical test described in Ref. [15].

The next step involves separately measuring the "dry" baseline characteristics of the test-rig including seal housing and additional supporting structures of the test-rig. The measurements utilize the "floating stator" method developed by Gilienicke [16]. Actual dynamic measurements include both the annular fluid reaction forces and the reactions from the test rig itself. To isolate the dynamic stiffness of the seals and the test rig, the operator applies dynamic excitations to the stator with no oil running through the test rig. These dry baseline results are then subtracted from the measured dynamic stiffness while testing with lubricant resulting solely in the fluid-film dynamic stiffness.

DYNAMIC RESULTS

Stiffness Coefficients

Figure 20 shows K_{tt} and K_{rr} versus ε_0 at ΔP = 2.07 bar and ω = 4krpm. As expected, at higher ε_0 values, K_{rr} is greater than K_{tt}, since the rotor has been displaced in the ε_0 direction, and the rotor is closer to the seal wall in the r direction. K_{tt} and K_{rr} increase as ε_0 increases for all clearances. K_{tt} and K_{rr} decrease as clearance increases. K_{rr} is well predicted for the 1X and 2X clearance seal up to ε_0 = 0.53. At ε_0 = 0.80, K_{rr} is 20% greater than predicted for the 1X clearance seal. K_{tt} is well predicted for the 1X and 2X clearance seal up to ε_0 = 0.53. At ε_0 = 0.80, K_{tt} is 20% greater than predicted for the 3X clearance seal. Also, at ε_0 = 0.80, measured K_{tt} is 50% greater than predicted for the 2X clearance seal.

Interestingly, measured K_{tt} and K_{rr} are negative at all eccentricity ratios for the 3X clearance seal. This seems to explain why it was difficult to hold the 3X clearance seal in the load-control mode. A negative stiffness would mean that the test rotor would be "sucked in" towards the stator wall. However, the model [1] predicts positive K_{tt} and K_{rr} for the 3X clearance seal. Predicted K_{tt} and K_{rr} are slightly positive for the 3X clearance at all eccentricity ratios.

For the 3X seal, recall that F_s was negative at ε_0 = 0.27, 0.53, ΔP = 2.07 bar and ω = 8krpm. This suggested that K_{rr} would also be negative. Measured K_{rr} is negative at these conditions. However, $\phi < 90°$ for Fig. 17a at ε_0 = 0.80 implied a positive K_{rr} versus the negative K_{rr} shown in Fig. 20.
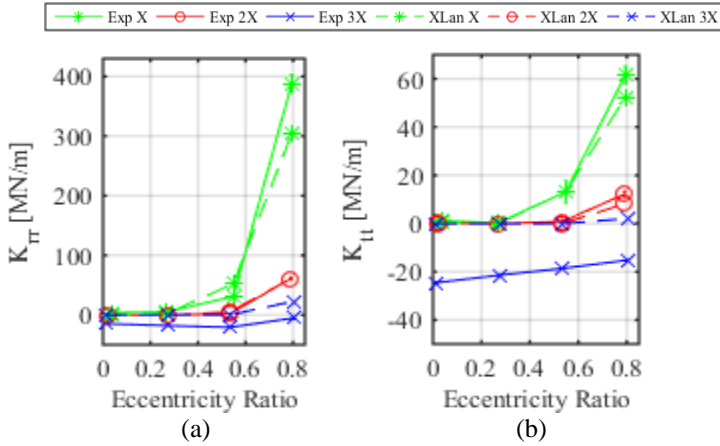
Figure 20. ΔP = 2.07 bar and ω = 4krpm (a) Measured and predicted K_{rr} versus ε_0. (b) Measured and predicted K_{tt} versus ε_0.

Figure 21a shows measured K_{tr} and K_{rt} versus ε_0 at ΔP = 2.07 bar and ω = 4krpm. For 1X and 2X clearance seals, $K_{rt} \cong -K_{tr}$ indicating strong destabilizing characteristics. Increasing the clearance from 1X to 2X decreases the cross-coupled stiffness. Increasing from 2X to 3X causes both K_{tr} and K_{rt} to become positive and no longer destabilizing; hence, the SBs are effective at the 3X clearance.

Figure 21b shows predicted K_{tr} and K_{rt} versus ε_0. The predictions agree well with test data for 1X and 2X clearance seals. For the 3X clearance seal, the model predicts different signs for K_{tr} and K_{rt} that could destabilize the pump. Measurements show that K_{tr} and K_{rt} are both positive, thus not destabilizing.

However, recall that measured K_{tt} and K_{rr} are negative at the 3X clearance. The 3X clearance seal 's negative direct stiffness coefficients would drop the pump's natural frequency, which would tend (by itself) to destabilize the pump rotor due to destabilizing forces of the impellers and other seals.
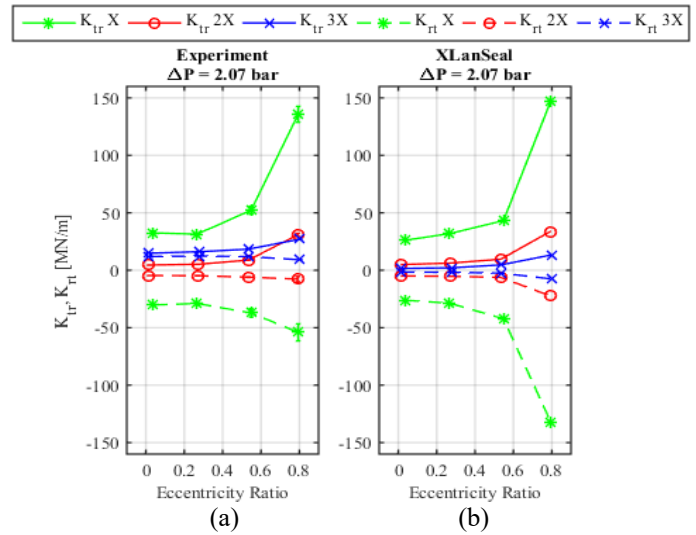

Figure 21. ΔP = 2.07 bar and ω = 4krpm (a) Measured K_{tr} and K_{rt} versus ε_0. (b) Predicted K_{tr} and K_{rt} versus ε_0.

Damping Coefficients

Figure 22 show C_{tt} and C_{rr} versus ε_0 at ΔP = 2.07 bar and ω = 2 krpm for all clearances. C_{rr} increases as ε_0 increases and C_r decreases. Note that for $\varepsilon_0 > 0.00$, C_{rr} is greater than C_{tt} since the rotor is moving closer to the seal wall in the r direction. C_{tt} and C_{rr} remain close to each other up to $\varepsilon_0 = 0.27$ and then start to diverge for all clearances. C_{rr} increases as ε_0 increases for all clearances. The predictions match the measurements very well for the 2X and 3X seals and the 1X seal out to $\varepsilon_0 \leq 0.57$. However, for the 1X clearance seal, predicted damping is markedly higher than measured at $\varepsilon_0 = 0.80$. For the 1X clearance seal, C_{tt} decreases up to $\varepsilon_0 = 0.51$ and then increases. The predictions follow the same trend but the predicted magnitude is higher. For the 2X and 3X clearance seals, C_{tt} increases as ε_0 increases, and the predictions closely match the measurements.

Figure 22. ΔP = 2.07 bar and ω = 2 krpm (a) Measured and Predicted C_{rr} versus ε_0. (b) Measured and Predicted C_{tt} versus ε_0.

Figure 23a shows measured and predicted C_{tr} versus ε_0 for all clearances at $\Delta P = 6.21$ bar and $\omega = 4$ krpm. Measured and predicted C_{tr} remain close to zero up to $\varepsilon_0 = 0.53$ and increases at $\varepsilon_0 = 0.80$ for all clearances. For the 1X clearance seal, predicted C_{tr} is larger than measured by about 5 times. For the 2X clearance seal at $\varepsilon_0 > 0.27$, predicted C_{tr} is larger than measured by about 10%. Predictions match measurements well for the 3X clearance seal.

Figure 23b shows C_{rt} versus ε_0. Measured and predicted C_{rt} remains close to zero up to $\varepsilon_0 = 0.53$ and increases at $\varepsilon_0 = 0.80$ for all the three clearance seals. For the 1X clearance seal, predicted C_{tr} is larger than measured by about 2 times. For the 2X clearance seal at $\varepsilon_0 > 0.27$ predicted C_{tr} is larger than measured by about 10%. Predictions match measurements well for the 3X clearance seal. Note that, for most of the test points C_{tr} and C_{rt} have the same sign. Therefore, they act as real dissipative damping and not gyroscopic damping.

Figure 23. $\Delta P = 6.21$ bar and $\omega = 4$ krpm (a) Measured and predicted C_{tr} versus ε_0. (b) Measured and predicted C_{rt} versus ε_0.

Virtual Mass

Figure 25 shows M_{tt} and M_{rr} versus ε_0 for all clearances at $\Delta P = 2.07$ bar and $\omega = 4$ krpm. Measured M_{tt} and M_{rr} decrease as ε_0 increases for the 1X clearance seal. They are largely independent of ε_0 for 2X and 3X clearance seals. For the 1X clearance seal, M_{rr} becomes negative with a large amplitude for $\varepsilon_0 = 0.80$. Note that a negative direct virtual mass term can increase the natural frequency of the rotordynamic system. For example, for the 1X clearance seal at $\varepsilon_0 = 0.8$, $\Delta P = 2.07$ bar and $\omega = 4$ krpm, comparing $M_{rr}\omega^2$ to K_{rr}, the resultant effecctive K_{rr} increases by about 9%.

For the 1X seal, predicted M_{rr} is about 3 times lower than predicted M_{rr} for the 2X and 3X clearance seals and independent of ε_0. The model predicts a negative M_{rr} at $\varepsilon_0 = 0.8$, and the data agrees. For the 2X and 3X clearance seals, predicted M_{tt} is about 3 times lower than measured. The model predicts a negative M_{tt} at $\varepsilon_0 = 0.53, 0.8$ while the data shows M_{tt} to be positive at all eccentricity ratios.

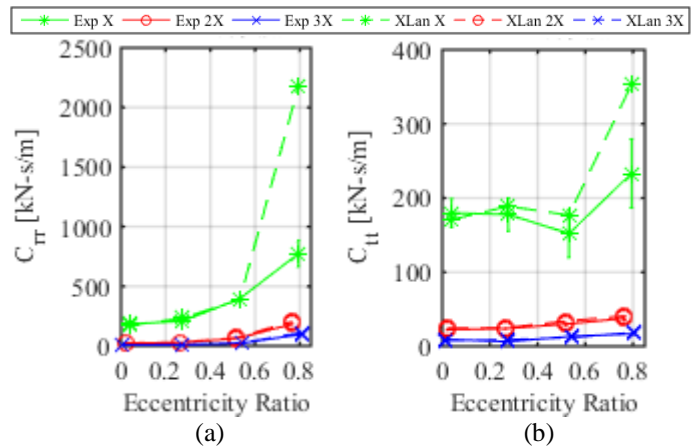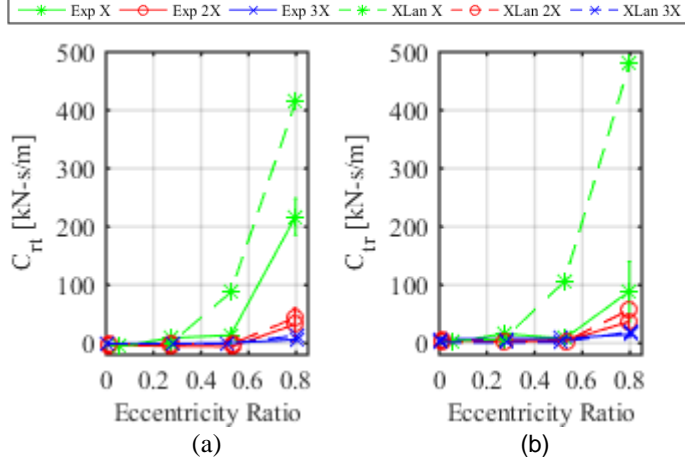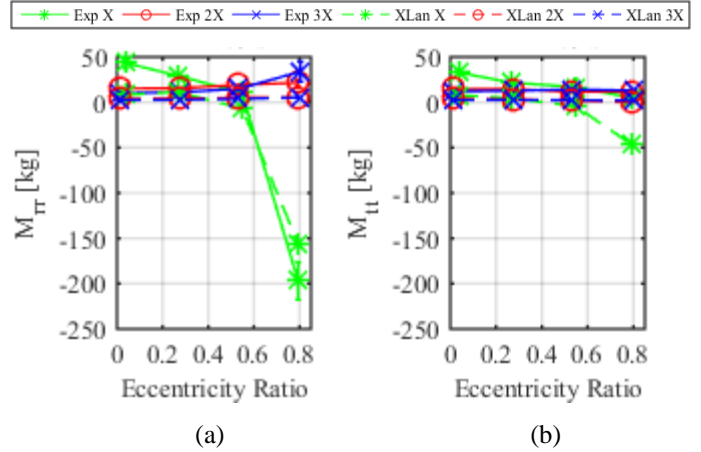**Figure 24.** $\Delta P = 2.07$ bar and $\omega = 4$ krpm (a) Measured and predicted M_{rr} versus. (b) Measured and predicted M_{tt} versus ε_0.

Figure 26 shows measured M_{tr} and M_{rt} versus ε_0 for all clearances at $\Delta P = 6.21$ bar and $\omega = 6$ krpm. For $\varepsilon_0 \leq 0.53$, the error bars are the same order of magnitude and comparable to measured data at all the conditions tested. Therefore, these findings are questionable.
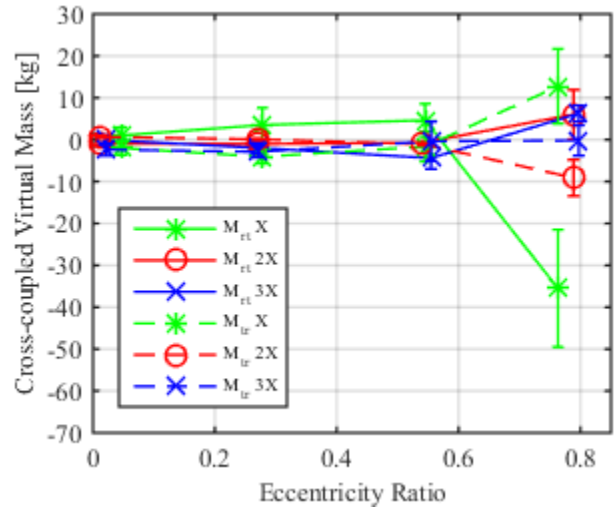

Figure 25. Measured M_{tr} and M_{rt} versus ε_0 at $\Delta P = 6.21$ bar and $\omega = 6$ krpm.

Table 1 shows the stability impact of M_{tr} and M_{rt} versus ε_0 for all clearances at $\Delta P = 6.21$ bar and $\omega = 6$ krpm. Note that (a) if M_{tr} and M_{rt} have the same signs, they do not impact the stability of the system (referred as 0), (b) if $M_{tr} > 0$ and $M_{rt} < 0$, they drive backward whirl (referred as Stabilizing FWD) and (c) if $M_{tr} < 0$ and $M_{rt} > 0$, they drive forward whirl (referred as Destabilizing FWD).

Table 1. Stability impact of M_{tr}, M_{rt} at ΔP = 6.21 bar and ω = 6krpm.

Clearance	ε_0			
	0.00	0.27	0.53	0.80
1X	Destabilizing FWD	Destabilizing FWD	Destabilizing FWD	Stabilizing FWD
2X	Stabilizing FWD	Stabilizing FWD	0	Destabilizing FWD
3X	0	0	0	Destabilizing FWD

Whirl Frequency Ratio

Figure 27 shows WFR [17] as function of ε_0 at ΔP = 4.14 bar and ω = 6 krpm. For the 1X and 2X clearance seals, WFR drops from approximately 0.5 to zero in moving from ε_0 =0.53 to ε_0 = 0.8. Note that this behavior resembles that of a plain journal bearing. For a clearance of 3X, since K_{tr} and K_{rt} have the same sign, WFR remains zero at all eccentricity ratios.

The model predicts well for 1X and 2X clearance. However, for the 3X clearance seal, measured K_{tr} and K_{rt} have the same signs producing WFR = 0. The model predicts different signs for K_{tr} and K_{rt} netting WFR $\cong$ 0.5. Although not shown here, WFR is independent of ΔP and ω for all the three clearances.
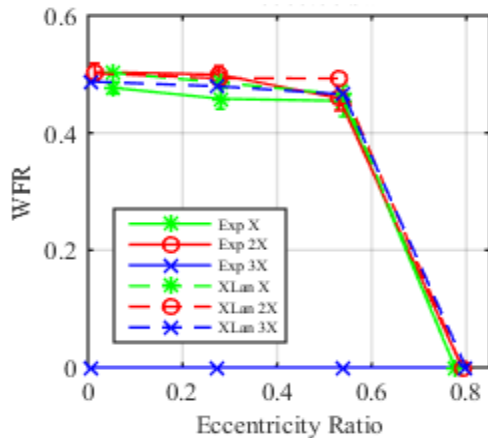

Figure 26. Measured and Predicted WFR versus ε_0 at ΔP = 4.14 bar and ω = 6 krpm.

Note for the 3X clearance seal, K_{rr} and K_{tt} are negative for most of the test cases. The pump's first critical speed depends on the direct stiffness. Negative direct stiffness values would drop the natural frequency, thus worsening stability. For an ESP, a negative stiffness could cause the rotor to rub against the stator wall. However, unless there are different signs for K_{tr} and K_{rt}, a seal will not cause a dynamic instability.

CONCLUSION

As expected, volumetric rate leakage $\dot{Q}$ increases as C_r and ΔP increase. $\dot{Q}$ increases as ε_0 increases.

Upstream circumferential velocity v_i is measured at one location with a pitot-tube (refer to Fig. 13 and 14 for location of inlet pitot-tube). As expected, v_i increases as C_r and ω increase.

Interestingly, v_i is influenced by the inlet velocity from the pre-swirl insert v_{insert} (refer Eq. (6)) to the extent that generally v_i (3X) > v_i (2X) > v_i (1X). As ΔP increases, v_i tends to trend more with v_{insert} and less with $R\omega$.

Notably for the 1X clearance seal at ε_0 = 0.27, $\phi \geq 90°$, an indication that fluid inertia effects are important [12]. For the 3X clearance seal, $\phi \cong 180°$ at ε_0 = 0.27, 0.53, ΔP = 2.07 bar and ω = 8krpm. This implies that there is no forward destabilizing force and that the centering force is negative.

As expected, for the 1X and 2X clearance seals, the applied static load F_s increases as ε_0 increases, and decreases as C_r increases. For the 1X and 2X clearance seals, measured applied static load is positive at all test conditions. For the 3X clearance seal, F_s is negative at ε_0 = 0.27, 0.53, ΔP = 2.07 bar and ω = 8krpm. This result agrees with the corresponding static load-deflection- attitude angle results.

The following points summarize the most important results of the dynamic measurements:

- For the 1X and 2X clearance seals, SBs have no impact on the rotordynamic coefficients.

- For the 3X clearance seal, measured direct stiffness coefficients are negative. Therefore: (a) the natural frequencies of the pump would drop, and (b) For sufficiently large negative direct stiffness values the rotor could be sucked in to the stator.

- For the 3X clearance seal, swirl brakes were effective in making K_{tr} and K_{rt} both positive. Thus the seal's cross-coupled stiffness coefficients are no longer destabilizing. This result becomes less important, since direct stiffness coefficients are negative.

- Measured and predicted C_{tr} and C_{rt} are both positive for all clearances at most of the test conditions an indication that they will act as direct damping as opposed to gyroscopic damping.

- For the 1X clearance seal, measured virtual mass coefficients are negative at some test conditions, an indication that they could increase the natural frequency of the pump.

- Predictions generally agree well with measurements. Most important discrepancies pertain to stiffness coefficients for the 3X clearance seal. The model [1] fails to predict: (a) negative direct stiffness coefficients, and (b) same signs for the cross-coupled stiffness coefficients.

REFERENCES

[1] Zirkelback, N., and San Andrés, L., (1996), "Bulk-Flow Model for the Transition to Turbulence Regime in Annular Seals," STLE Tribology Transactions, Vol 39 No 4, P. 835-842.

[2] Lomakin, A., 1958, "Calculation of Critical Number of Revolutions and the Conditions Necessary for Dynamic Stability of Rotors in High-Pressure Hydraulic Machines When Taking Into Account Forces Originating in Sealings," *Journal for Power and Mechanical Engineering (In Russian),* **14**.

[3] Pinkus, O., and Sternlicht, B., 1961, *Theory of Hydrodynamic Lubrication*, New York: McGraw-Hill.

[4] Childs, D., Norrbin, C., and Phillips, S., 2014 "A lateral rotordynamics primer on electrical submersible pumps (ESP's) for deep subsea applications," in Proceedings of the *30th Pump User's Symposia*, .

[5] Childs, D.W., 2013, *Turbomachinery Rotordynamics with Case Studies*, Wellborn, Texas: Minter Spring Publishing.

[6] Black H.F., Allaire, P., and Barret, L., 1981, "Inlet Flow Swirl in Short Turbulent Annular Seal Dynamics," in *Ninth International Conference on Fluid Sealing*, Noordwijkerhout, Netherlands, pp. 141-152.

[7] Benckert, H., and Wachter, J., 1980 "Flow Induced Spring Constants of Labyrinth Seals for Applications in Rotor Dynamics," in *Proceedings of the 1st Workshop on Rotordynamic Instability Problems in High-Performance Turbomachinery*, College Station, Texas, Texas A&M University, pp 189-212.

[8] Massey, I., (1985), "Subsynchronous Vibration Problems in High-Speed Multistage Centrifugal Pumps," Proceedings, 14th Turbomachinery Symposium, organized by Texas A&M University, pp. 11-16.

[9] Najeeb, O.A., and Childs, D.W., 2017, *Static and Rotordynamic Analysis of a Plain Annular (Liquid) Seal in The Laminar Regime With a Swirl Brake for Three Clearances*, Texas A&M University, College Station, Texas.

[10] Kaul, A., 1999, "Design and Development of a Test Setup for the Experimental Determination of the Rotordynamic and Leakage Characteristics of Annular Bushing Oil Seals"*, College Station, Texas: Texas A&M University.

[11] Moreland, A. J., 2016, "Moreland - Effect of Eccentricity and Pre-swirl on Smooth Stator_Grooved Rotor Liquid Annular Seals, Measured Static and Dynamic Results," M.S. Thesis, Texas A&M University, College Station.

[12] You HI, Lu SS. The Effect of Fluid Inertia on the Operating Characteristics of a Journal Bearing. ASME. *J. Tribol*. 1988;110 (3):499-502.

[13] Rouvas, C., and Childs, D.W., 1993, "A Parameter Identification Method for the Rotordynamic Coefficients of a High Reynolds Number Hydrostatic Bearing," *Jounal of Vibration and Acoustics,* **115**, pp. 264-270.

[14] Childs, D.W., and Hale, K., 1994, "A Test Apparatus and Facility to Identify the Rotordynamic Coefficients of High-Speed Hydrostatic Bearings," *Journal of Tribology,* **116**, pp. 337-343.

[15] Beckwith, T., Marangoni, R., and Lienhard, V., 2007, *Mechanical Measurements*, Pearson Education, Inc, Upper Saddle River, NJ.

[16] Glienicke, J., 1966-67, "Experimental Investigation of the Stiffness and Damping Coefficients of Turbine Bearings and Their Application to Instability Prediction," in *Proceedings of IMechE 1966-67*, **181**, pp. 116-129.

[17] San Andres, L., 1991, "Effect of Eccentricity on the Force Response of a Hybrid Bearing," *Tribology Transactions*, **34**, pp. 537–544.